== SOLIDS AND LIQUIDS ===

PHYSICAL PROPERTIES OF ZIRCONIUM DIBORIDE AT TEMPERATURE 2500-5000K

© 2024 S. V. Onufriev^{a,*}, A. I. Savvatimskiy^{a,b,**}

^aJoint Institute for High Temperatures of the Russian Academy of Sciences, Moscow 125412, Russia ^bLebedev Physical Institute of the Russian Academy of Sciences, Moscow 119991, Russia *e-mail: s-onufriev@yandex.ru

**e-mail: savvatimskiy.alexander@gmail.com

Received June 02, 2024

Revised June 30, 2024

Accepted July 01, 2024

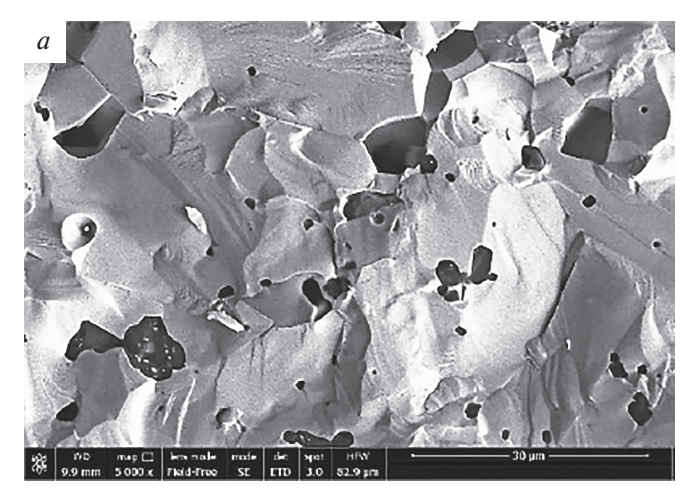
Abstract. Results of measuring the properties of zirconium diboride ZrB_2 in the temperature range of 2500–5000 K are presented: enthalpy, heat of fusion, heat capacity, specific electrical resistivity. Data for the liquid phase were obtained for the first time. The study was conducted using microsecond current pulse heating — Lebedev's "exploding conductors" method on sintered plates of ZrB_2 . The measured melting onset temperature of the diboride, 3400–3440 K, agrees with the B-Zr phase diagram. It was established that at 3000 K the heat capacity $C_p = 2 \text{ J/g} \cdot \text{K}$ is twice as high as the extrapolated low-temperature reference data, and in the liquid phase, there is a monotonic decrease in C_p from 2 to 1.5 $\text{J/g} \cdot \text{K}$ (at 5000 K). To explain the discrepancies, a hypothesis about the determining role of Frenkel defects in the melting region of rapidly heated substance is used.

DOI: 10.31857/S004445102411e075

1. INTRODUCTION

Recently, ultra-high temperature materials with melting points of 3300 K and above, operational at temperatures up to 2000–2300 K [1] have been actively studied. These materials find applications in rocket and space technology and nuclear power engineering. Substances with such properties include carbides, nitrides, metal borides, among which zirconium and hafnium borides are considered the most resistant to oxidation. Zirconium diboride ZrB₂ is a chemical compound with a molar mass of 112.846 g/mol, having high electrical and thermal conductivity, high melting point (approximately 3500 K), and possessing high strength, hardness, and chemical resistance. Zirconium boride ZrB2 is one of the lightest compounds (calculated density 6.09 g/cm³), used as thermal protection in aviation and astronautics. It is also known that due to their high neutron capture cross-section, borides are used in nuclear technology as materials for control rods and for protection against nuclear radiation [2]. Due to its resistance to molten metals and high thermal conductivity, zirconium diboride is used for manufacturing thermocouple tips in steel production. However, despite the demand for zirconium diboride, its properties at high temperatures have not been sufficiently studied. There is still a lack of reliable experimental data on enthalpy, heat capacity C_p and electrical resistivity of the solid phase $\rm ZrB_2$ at temperatures close to the melting point, for which only estimated data are available. Moreover, the literature completely lacks experimental data on physical properties $\rm ZrB_2$ in the liquid state. To obtain this information, we conducted an experiment with rapid (microsecond) heating of boride plates $\rm ZrB_2$ by an electric current pulse.

Investigation of high-temperature properties of refractory and super-refractory substances with melting temperatures above 3000 K is expedient to conduct using pulsed methods of current or laser heating. These methods allow studying the solid phase, melting region, and liquid phase with heating times ranging from microseconds to hundreds of milliseconds. In our opinion, the current pulse heating method is preferable, as it provides volumetric heating which, unlike surface laser heating, can be uniform under certain conditions, ensuring a homogeneous state of matter. The most convenient method, not requiring corrections for



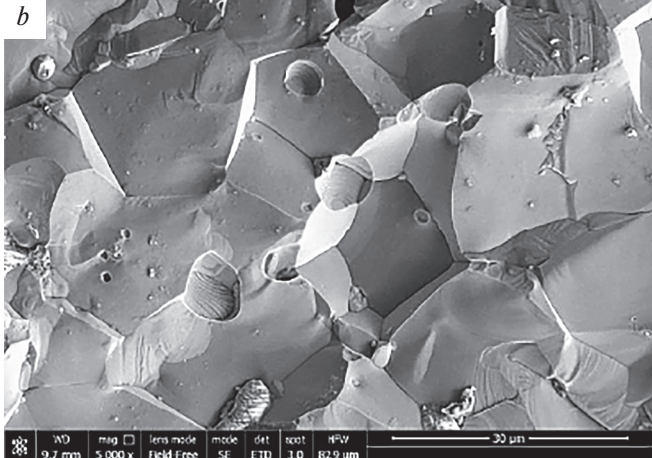


Fig. 1. a – Microstructure of sample No. 1. b – Microstructure of sample No. 2

radiation heat losses, is the microsecond-duration current pulse heating method.

This is the so-called "explosive" method of conductor heating [3], pioneered by Sergey Vladimirovich Lebedev (1913–1990).

The authors effectively continue similar experimental work using this method at a new level: utilizing digital technology for recording fast processes.

The method allows obtaining a uniform state of the conductor during heating under specific relationships between conductor thickness (usually tens to hundreds of micrometers), its electrical conductivity, current density, and heating time [4, 5]. With short heating time, the black body model — cylindrical [5] or wedge-shaped [6] — is preserved in both solid and liquid phases, allowing measurement of emissivity and true temperature of the substance.

It should be noted that the melting temperature T_m of a substance is the same for both stationary heating and rapid microsecond heating. This is confirmed in many of our experiments for both metals and carbides. However, some studies [7] claimed that during rapid heating, metal "overheating" may occur, with its melting temperature increasing by "hundreds of degrees". Our direct experiment [8] with rapid microsecond heating of tantalum foil (in the form of a black body model) showed that the melting temperature of tantalum remains equal to its stationary value. At the same time, it was established that with heating duration of several microseconds, the temperature difference between the surface of the melting sample and its core is about 20 K [6]. This

difference equalizes across the conductor's cross-section in approximately $0.2 \mu s$.

Meanwhile, the study of polymorphic transitions shows that the measured transition temperature depends on its nature: in the case of martensitic transition, for example, the $\alpha-\beta$ transition in zirconium, its temperature and input energy remain the same as in stationary heating [4]. In the case of slow diffusion transition, for example for nichrome X20N80, the transition temperature shifted 1000 K above the stationary value [9].

In addition to these effects, during rapid current heating, abnormally high heat capacity growth and increased electronic emission of metals before melting were discovered [3]. Presumably, the cause of the abnormal heat capacity growth may be the appearance of Frenkel pair defects (interstitial atom + vacancy) in the substance volume shortly before melting, which contribute to the lattice destruction during melting [3]. The formation of such a pair defect in metal requires energy significantly higher than for vacancy formation, which should lead to additional heat capacity growth compared to stationary heating, when mainly vacancies are formed. Abnormal heat capacity growth near the onset of solid phase melting is also observed in the case of graphite [10] and carbides [11] heating. The lattice reconstruction causes restructuring of the electronic subsystem, which may cause abnormal growth of electronic emission in this state region.

Ultra-refractory ceramics, which includes zirconium diboride, is manufactured using three main methods: 1) powder pressing and sintering

method; 2) sputtering method, such as magnetron sputtering; 3) chemical vapor deposition method. Recently, the sol-gel method has also been developing [12]. The grain size, porosity of ceramics, and selection of the thickness of studied samples depend on the manufacturing method. The first method typically produces ceramics with grain sizes of tens of micrometers, which necessitates the use of relatively massive samples hundreds of micrometers thick. The second method allows obtaining samples with grain sizes of tenths of micrometers, making it possible to study film samples several micrometers thick. The third method also allows obtaining film coatings with small grain sizes. The sol-gel technology provides very small grain sizes.

In this work, sintered samples of zirconium diboride with a thickness of 100–120 µm were studied.

2. MEASUREMENT METHOD AND SETUP

The measurement method and setup description, including the description of the high-speed pyrometer, are presented in several publications [4, 13–15]. The current pulse heating the sample is formed by discharging a high-voltage capacitor bank through a ballast resistor and sample connected in series. A digital oscilloscope records the current I through the sample, voltage u across the sample, and pyrometer signal U_p .

Here we present the relationships necessary for calculating the following quantities determined in the experiment.

1. The Joule heating energy dissipated in the sample (enthalpy),

$$E(t) = \frac{1}{m} \int_0^t I(t) U(t) dt \approx \frac{1}{m} \sum_{i=0}^k I(t_i) U(t_i) \delta t, \quad (1)$$

where m – sample mass, $U(t_i) = u(t_i) - u_{ind}(t_i)$ – voltage drop across the active resistance of the sample, $u_{ind}(t_i)$ – inductive component of voltage across the sample, $k = t/\delta t$, where δt – sampling period of the digital oscilloscope. With a standard value of $\delta t = 2$ ns and oscilloscope sweep of 20 μ s, the number of points per sweep will be $k = 10^4$.

2) Sample temperature [14]

$$T(t) = \frac{C_2}{\lambda \ln \left[\frac{U_0 \varepsilon_{\lambda n} \tau_{\lambda}}{U_n(t) \varepsilon_{\lambda n}^0 \tau_{\lambda}^0} \left(\exp(\frac{C_2}{\lambda T_0}) - 1 \right) + 1 \right]}, \quad (2)$$

where C_2 is the constant in Planck's formula, U_0 and $U_p(t)$ are pyrometer signals during calibration and from the sample, $\varepsilon_{\lambda n}$ and $\varepsilon_{\lambda n}^0$ are normal spectral emissivity of the sample surface and tungsten ribbon of the SI-10-300 lamp, $\tau_{\lambda} = \prod \tau_{i\lambda}$ is the total transmission coefficient of the upper plate of the cell $(\tau_{1\lambda})$, see below) and protective glass $(\tau_{2\lambda})$ — elements that are removed during pyrometer calibration, $\tau_{\lambda}^0 \approx 0.92$ is the transmission coefficient of the temperature lamp window, $T_0 = 2515$ K is the temperature of the SI-10-300 lamp tungsten ribbon at which pyrometer calibration is performed. The transmission coefficients $\tau_{i\lambda}$ were measured using a Shimadzu UV-240 spectrophotometer at the pyrometer wavelength of 856 nm.

3) Specific isobaric heat capacity [15]

$$C_{p}(T) = \frac{E(T(t_{i} + n\tau)) - E(T(t_{i}))}{T(t_{i} + n\tau) - T(t_{i})},$$
 (3)

where E(T(t)) is the Joule heating energy (1), t_i and $t_i + n\tau$ are the beginning and end of the *i*-th time interval, n is the specified number of points. Usually 150 points are taken, corresponding to a temperature interval of 150–250 K. The obtained value C_p refers to the mean temperature of the interval

$$T_{ref} = [T(t_i + n\tau) + T(t_i)]/2.$$

4. Specific electrical resistivity, referred to the initial sample dimensions,

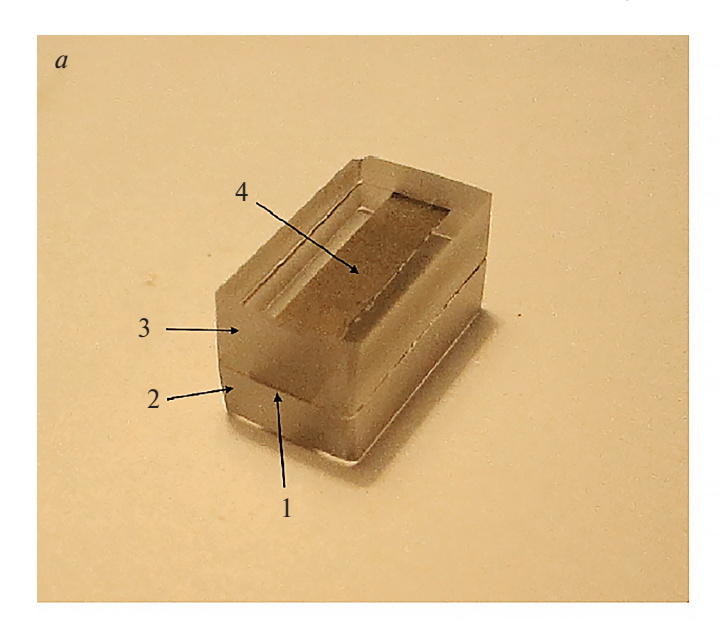
$$\rho(T) = R(T) \frac{S_0}{L_0},\tag{4}$$

where R is the active resistance of the sample, S_0 and L_0 are initial cross-sectional area and length of the sample.

The uncertainties of these values are 7–10% for energy depending on sample uniformity and quality (for metals this uncertainty is 5%), 15% for heat of fusion, 80–100 K for temperature 4000 K without accounting for emissivity uncertainty, 20% (for solid phase) and 30% (for liquid phase) for heat capacity, 7–10% for specific electrical resistivity. The temperature measurement uncertainty, considering emissivity uncertainty, is expressed by the formula

$$\frac{\delta T}{T} = \frac{\lambda T}{C_2} \frac{\delta \varepsilon_{\lambda n}}{\varepsilon_{\lambda n}},$$

where notations are the same as in formula (2).



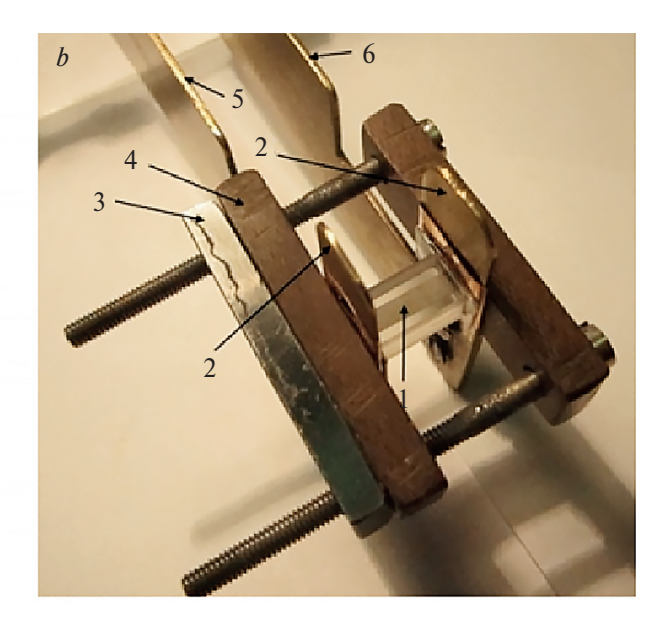


Fig. 2. a — Quartz glass cell with sample ZrB_2 : 1 — end face of the plate ZrB_2 (flush grinding with quartz glass ends); 2 — bottom plate (thickness 3.3 mm); 3 — top plate (thickness 4 mm); 4 — plate ZrB_2 with width 4 mm. b — Cell with sample clamped in current leads: 1 — diboride sample inside quartz cell; 2 — brass current leads; 3 — steel plate; 4 — textolite plate; 5, 6 — brass electrodes

3. SAMPLES

Samples of ZrB_2 of two different manufacturers: sample No. 1 and sample No. 2 were studied. Table 1 shows the main characteristics of the initial workpieces used to manufacture the samples.

These workpieces were cut using electrical discharge machining into plates $0.5 \times (3-4) \times 15 \text{ mm}^3$, which were then polished with diamond pastes to the size of $(0.1-0.12)\times(3-4)\times15 \text{ mm}^3$.

Analysis of the microstructure of fracture surfaces of samples No. 1 and No. 2, as well as evaluation of the elemental composition of this surface for sample No. 1 using EDS (energy dispersive spectroscopy) was performed on a Nova NanoSem 650 scanning electron microscope using a secondary electron detector, annular backscattered electron detector, and EDAX energy-dispersive analysis system. The characteristic appearance of the sample fracture microstructure is shown in Fig. 1.

The fracture surface of sample No. 1 (Fig. 1a) has predominantly transcrystalline character and consists of tightly adjacent grains with sizes of $5-20 \mu m$. The fracture surface contains inclusions (dark colored) and cavities, apparently formed due to the chipping of some of these inclusions. Their sizes range from submicron to micron, the volume content of dark inclusions is limited (3-3.5%). The

assessment of chemical elements content both in inclusions and when scanning areas of $100 \times 50 \ \mu m^2$ is shown in Table 2. Impurity elements Fe, Co, and Mg are concentrated mainly in dark inclusions, and their concentrations vary greatly. However, the approximate total content of these elements can be estimated at less than 0.15 wt%. Aluminum and tungsten in small quantities are consistently detected across the entire fracture surface.

According to Table 2, the mass fraction of ZrB_2 in sample No. 1 (area estimation) was 98,7%. For these areas, the ratio $B/Zr \approx 2.72$, for dark inclusions $B/Zr \approx 17.1$, i.e., the sample contained ZrB_2 and possibly free boron, ZrB_{12} and borides of impurity metals.

The fracture surface of sample No. 2 (Fig. 1b) has a mixed character — grain boundary and intragranular. The surface shows tightly adjacent grains with linear dimensions of $5-30~\mu m$, as well as individual inclusions of submicron and micron sizes. Table 3 shows the mass fraction of impurities in sample No. 2 according to the manufacturer's certificate. The proportion ZrB₂ is 99.898 wt%.

X-ray phase analysis of sample No. 2 showed that it consists of 99.3% hexagonal ZrB_2 and 0.7% monoclinic ZrO_2 and contains 66.3 at% boron, 33.3 at% Zr and 0.4 at% oxygen. Thus, this sample has higher purity,

Number of sample Initial blank disk Material purity, wt% Density, g/cm³ Porosity*, % diameter 85 mm thickness 16 mm. 98 ZrB₂ 5.607 7.9 sintering method diameter 50 mm Not less than 99.5 2 thickness 3 mm. 5.858 3.8 ZrB_2 sintering method

Table 1. Information about blanks for sample manufacturing

Note.* – density ZrB_2 6.09 g/cm³ [16].

Table 2. Element content in sample No. 1

	Area 100 × 500 μm ²		Dark inclusion	
Element	Wt%	At%	Wt%	At%
В	24.03	72.61	63.67	93.01
Al	0.41	0.50	1.42	0.83
W	0.90	0.16	1.23	0.11
Zr	74.65	26.73	31.38	5.43
Fe	_	_	0.50	0.14
Co	_	_	1.80	0.48

lower porosity, and stoichiometric composition (B/Zr = 1.99) compared to sample No. 1.

According to reference books, zirconium diboride (brittle at room and higher temperatures) becomes plastic at T > 1400 K. In order to clamp a thin diboride plate at the ends in the current leads (current is passed along the sample), it was previously glued into a cell consisting of two glass plates $(3.3 - 4) \times 8 \times 15$ mm³, the view of which is shown in Fig. 2a. The cell was placed between the current leads of the high-voltage installation and was clamped through copper and indium gaskets (Fig. 2b). The temperature was measured on the flat surface of the sample through the upper quartz glass, the transmission of which was taken into account. UV-curing Bohle adhesive was used for bonding.

4. EXPERIMENTAL RESULTS

Fig. 3 shows a typical view of oscillograms (10 μ s sweep) obtained in the experiment with ZrB₂.

The oscillograms show no sharp bends or jumps, indicating that the heating of the sample in the solid phase, its melting and heating of the liquid phase occurred without destruction of the sample or cell. This indicates that the cell design and heating method (volumetric heating) allow experiments with brittle samples, and indirectly indicates heating uniformity.

Table 3. Mass fraction of impurities in sample No. 2

Mg	Al	Si	Ca	Ti	Cr
0.0055	0.0012	0.0026	0.0066	0.0059	0.0043
Mn	Fe	Co	Ni	Hf	W
0.002	0.027	0.0029	0.004	0.0064	0.034

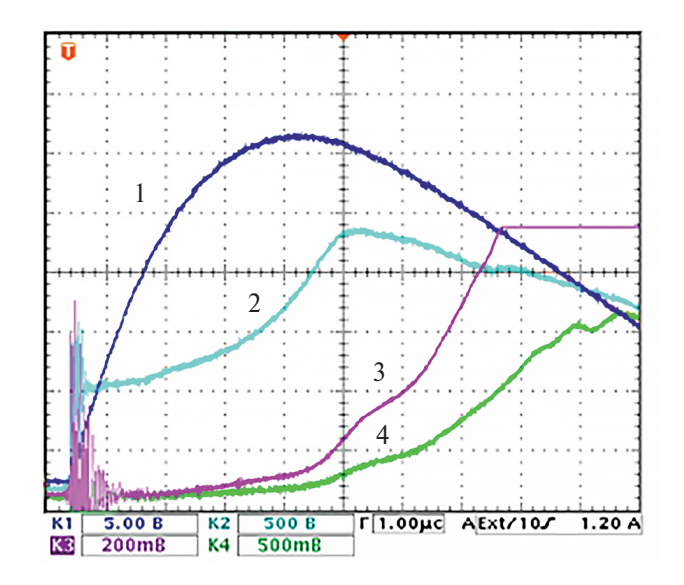


Fig. 3. Oscillograms: 1 - current (maximum value 29 kA); 2 - voltage across the sample u; 3 - signal $U_p(t)$ pyrometer; 4 - pyrometer signal at low sensitivity. Pyrometer signal recording is used on two channels to expand the dynamic range of the pyrometer [17]

The high heat resistance of the samples ZrB₂, due to their high thermal conductivity [1], also plays a role.

On oscillograms 3, 4 between the 5th and 7th microseconds from the start of the sweep, an inclined "melting plateau" is observed: at some point, the rate of change in the pyrometer signal drops, although energy continues to be released in the sample. It is natural to define this moment as the beginning of sample melting. After the sample is completely melted, the rate of temperature increase of the liquid phase increases. Thus, a melting plateau appears, which allows determining the temperatures of melting onset and completion.

Fig. 4 shows the heating thermograms of samples No. 1 and No. 2 with determination of phase transition temperatures — melting. The thermograms are calculated using formula (2).

To determine the melting start and end points, the thermogram sections near the melting region and the melting region itself are approximated by straight lines, and the intersection points of the angle bisectors with the thermogram are found, as shown in Fig. 4. These special points of the thermogram are equidistant from the straight lines approximating adjacent sections of the thermogram relating to different phases. These points are taken as the melting start and end points.

For sample No. 1 and sample No. 2, the melting start temperatures of 3440 and 3400 K respectively (and separately melting end temperatures of 3720 and 3750 K) agree within measurement error margins.

The pyrometer records the brightness temperature of the sample surface at a wavelength of $\lambda = 856$ nm. To determine the true temperature and construct thermograms (Fig.4), it is necessary to know the normal emissivity $\varepsilon_{\lambda n}$. As known, $\varepsilon_{\lambda n}$ changes with wavelength and temperature increase and depends on the composition and surface condition of the sample. Literature data is typically used. For ZrB₂ such data are provided in [18–24]. In work [18], bulk samples of ZrB₂ with high porosity of approximately 24% (density 4.5 g/cm³), obtained by cold pressing were studied. Measurement of normal emissivity at a wavelength of 650 nm showed that it linearly decreases from 0.76 to 0.68 with temperature increase from 1300 to 1900 K. Studies on a sintered compact sample of zirconium diboride containing 3% tungsten and 8% oxygen were performed in work [19], whose results qualitatively contradict the results of work [18]: in [19], the emissivity at the

same wavelength increases from 0.72 to 0.84 with temperature rise from 1604 to 2480 K, rather than decreasing as in [18]. In [19], for our wavelength of 856 nm in the same temperature range, the value of $\varepsilon_{\lambda n}$ increases from 0.61 to 0.77.

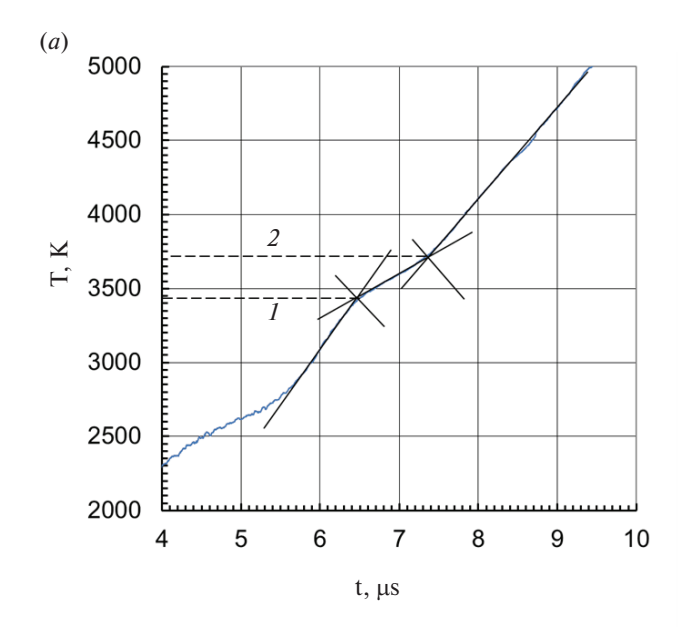
A series of studies was performed on powder samples ZrB₂, applied to a heated metal conductor. In work [20], the emissivity ZrB₂ was studied in the form of a coating on a tantalum rod. It was established that for $\lambda = 655$ nm in the temperature range 900-1700 K it is constant and equals 0.7. Information about the purity of the coating material and its porosity is absent in [20]. Considering measurement errors, it can be assumed that the data from works [18] and [20] do not contradict each other. The research results [20,21] are presented in [23]. It was established that for $\lambda = 655$ nm in the temperature range 1073 - 1873 K, the emissivity of ZrB₂ slightly increases from 0.89 to 0.91. The cause of high emissivity values obtained in [21, 22] could be methodological errors considered in work [24] – radiation from heated parts of the setup entering the measurement path.

Thus, we see that information about emissivity is mainly provided for wavelengths of 650–655 nm. They are contradictory and limited to relatively low temperatures. Work [19] is the only one where studies were performed in the spectral range of 0.4–5 μ m, covering our wavelength of 856 nm. Taking into account the totality of information about emissivity, in the present work, it is assumed that the emissivity for solid and liquid phases of diboride at a wavelength of 856 nm equals 0.7. Temperature calculations in this work were performed for this emissivity. As seen from formula (2), the calculated temperature under otherwise equal conditions will decrease with increasing $\epsilon_{\lambda n}$ and conversely increase with decreasing $\epsilon_{\lambda n}$.

Experiments with two types of samples gave approximately the same results: repeatable heating thermograms (Fig. 4), repeatable temperature dependencies of heating energy dissipated in the sample (enthalpy) (Fig. 5), dependencies of heat capacity (Fig. 6) and specific electrical resistivity (Fig. 7).

For sample No. 1, data were obtained in a larger temperature range, therefore temperature dependencies of properties for this type of samples are mainly analyzed.

Fig. 5 shows the curves of energy change E of Joule heating dissipated in the sample (enthalpy)



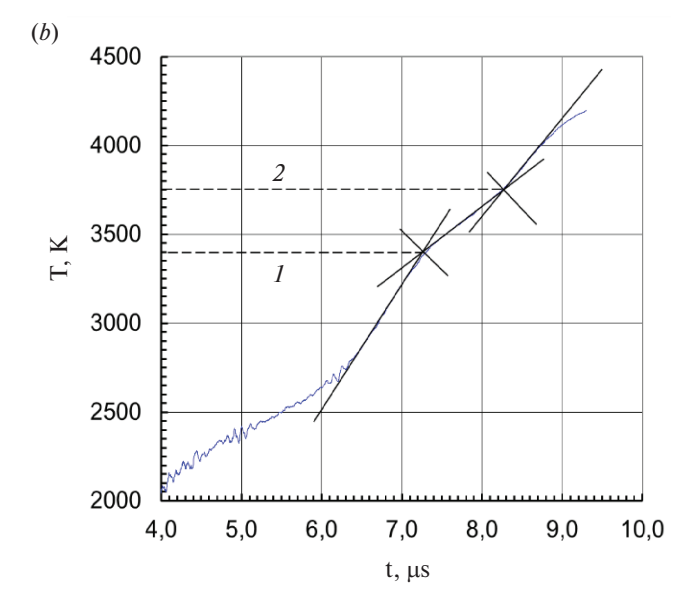


Fig. 4. a — Heating thermogram of sample No. 1 with determination of melting interval: 1 and 2 — beginning and end of melting (3440 and 3710 K). Heating rate is higher than for sample No. 2. b — Heating thermogram of sample No. 2 with determination of temperature melting interval: 1 and 2 — beginning and end of melting (3400 and 3750 K)

versus temperature. On this graph, dashed lines 5, 6 indicate the melting start and end temperatures of ZrB₂ found from Fig. 4*b*, and lines 7, 8 show the corresponding energies.

Note that the heating energy for the liquid region ZrB₂ (above 4000 K) measured in the experiment is much higher than the calculated values (lines 3 and 4). For the temperature region near 2500 K, the picture is reversed: the experiment gives lower heating energy values.

Fig. 6 shows the temperature dependencies of heat capacity at constant pressure, C_p , for zirconium diboride before melting from 2 to 2.5 J/(g • K) with temperature increase from 3000 to 3300 K and a sharp decrease after melting from 2.5 to $\approx 2 \text{ J/(g • K)}$ with temperature increase from 3800 to 4000 K. According to the authors, these effects are associated with the formation of Frenkel defects in the solid phase before melting and their disappearance after melting.

Note that the increase in heat capacity (as well as its decrease after melting), according to the measurement conditions considered in work [15], should be considered only outside the temperature interval 3340–3810 K.

Let's note another feature of heat capacity observed for zirconium diboride and previously observed for carbides: the decrease in C_p after melting

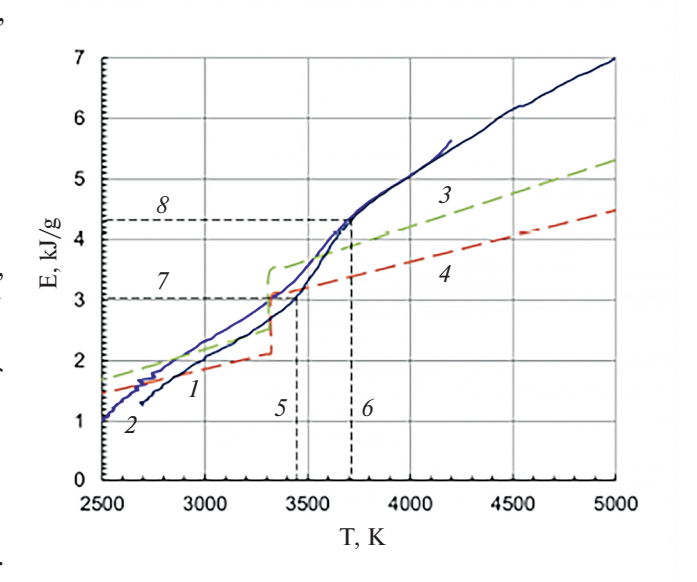
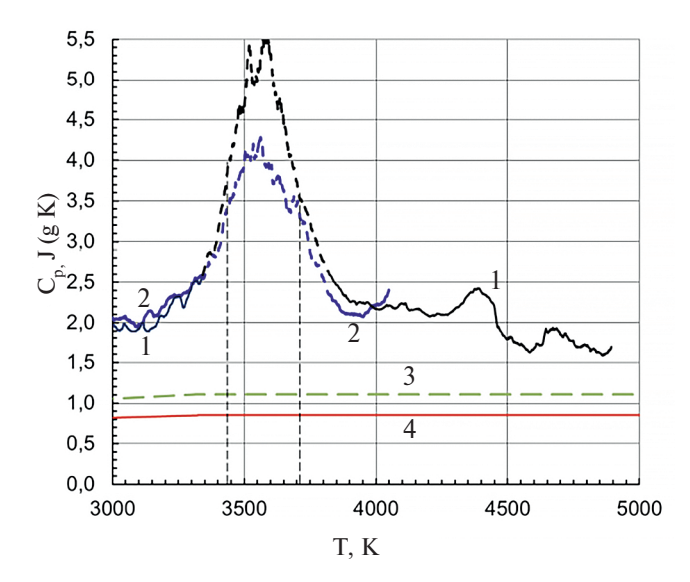
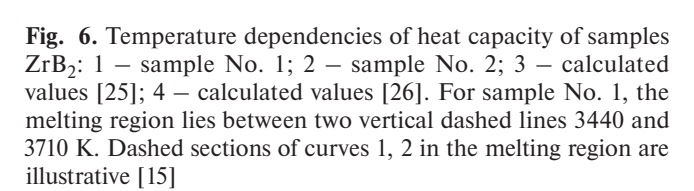


Fig. 5. Temperature dependencies of specific Joule heating energy for samples ZrB_2 (enthalpy): 1 – sample No. 1; 2 – sample No. 2; 3 – calculated data [25]; 4 – calculated data [26]; 5 and 6 – temperatures of beginning T_{m1} and end T_{m2} of melting of sample No. 1; 7 and 8 – energies corresponding to these temperatures. Heat of melting $\Delta E = 1.27$ kJ/g (143 kJ/mol)

below C_p of solid state, before melting. This can be explained, on one hand, by the fact that the studied samples were not annealed before the experiment. Consequently, they carried all initial defects, while after melting most of these defects were "annealed"





out" in the melting region. On the other hand, during the time after the end of melting (about 2 μ s), Frenkel defects presumably disappear in the liquid.

Sample No. 1 was studied at a higher heating rate, which allowed recording the heat capacity of the liquid phase at a higher temperature.

Fig. 7 shows temperature dependencies of specific electrical resistivity of zirconium diboride. Dashed lines 3 and 4 show the temperatures of beginning and end of melting of sample No. 1, and 5 and 6 — the resistance of the sample in solid phase before melting and in liquid phase after melting (referred to initial sample dimensions).

5. DISCUSSION OF RESULTS

5.1. Assessment of Pressure Generated During Pulse Heating

Heating and expansion of the sample in a glass cell leads to the appearance of pulse pressure in the sample. To estimate this pressure, we will neglect the adhesive layer separating the sample from the cell plates and use the estimation of dynamic pressure P_d , arising from the movement of the piston (sample) in the medium (glass) [11, 17, 27]:

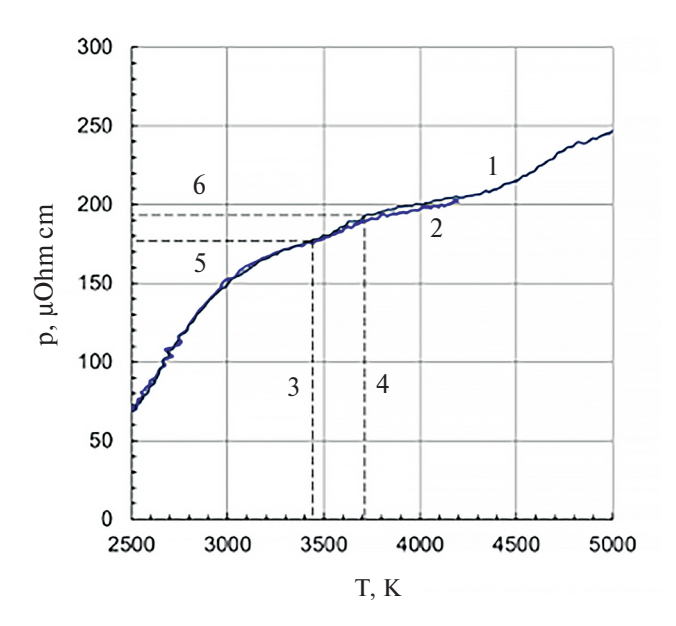


Fig. 7. Dependencies of specific electrical resistivity of samples ZrB₂ on temperature. Specific resistance is related to the initial dimensions of samples: 1 – sample No. 1; 2 – sample No. 2. Melting region 3–4 (3440–3710 K) is marked with vertical dashed lines

$$P_d = zU_b, (5)$$

where $z = \gamma_s c$ — wave resistance of the medium, γ_s and c – density of the medium and sound velocity in the medium in which the sample expands, U_h velocity of sample-medium boundary movement during sample expansion. Sample expansion in thickness is symmetric, therefore half of this expansion needs to be considered. In solid phase, thermal expansion coefficient ZrB2 for temperature range from 293 K to T_m equals $\alpha = 8.4 \cdot 10^{-6} \text{ K}^{-1}$ [28]. In liquid phase, expansion coefficient is approximately 3\alpha. We will assume that during melting the volume increases by approximately 3% (as for metals [29]) and that the increase in sample volume during melting and liquid phase volume growth occur only due to sample thickness increase. Then when heating the sample to 5000 K in 8 µs, we get average boundary movement velocity of 0.73 m/s and average pressure $P_d \approx 10$ MPa with wave resistance of quartz glass $z = 1.32 \cdot 10^7 \text{kg/(m}^2 \cdot \text{s)}$ [16]. The highest pressure occurs during sample melting, during which the boundary moves at the highest velocity $U_b \approx 2$ m/s, giving pressure $P_d \approx 26$ MPa (estimates are given for infinitely thick quartz plates). Electromagnetic pressure at maximum current density $8 \cdot 10^{10}$ A/m², equal to zero on the sample surface, in its middle is about 7 MPa [11]. As a result,

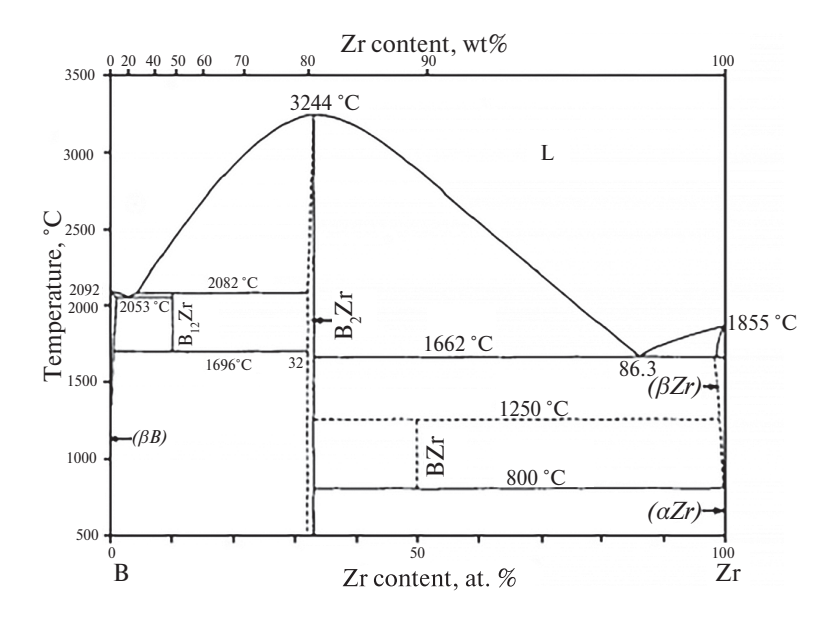


Fig. 8. Phase diagram of the system B–Zr (adapted from work [32])

we get that pressure in the sample could temporarily reach 30 MPa. Such pressure level does not affect the values of enthalpy and heat capacity of the sample [15, 30].

Quartz plates had a thickness of 3.5 mm. When the disturbance caused by sample expansion reaches the free surface of the plate, a release wave is formed [31], moving in the opposite direction and leading to pressure reduction in the glass and sample. At the speed of sound in quartz glass $5.9 \cdot 10^3$ m/s the release wave will reach the sample 1.2 μ s after heating begins, causing a pressure decrease while it is still in solid phase. Further heating of the sample occurs under the influence of release waves that reduce pressure.

5.2. Melting ZrB₂

For analysis and discussion of results, the phase diagram of the system Zr–B, shown in Fig. 8 [32], is necessary.

According to the diagram, two chemical compounds are formed in the system Zr-B zirconium diboride ZrB_2 and dodecaboride ZrB_{12} . Unlike zirconium carbide or nitride, which have a wide homogeneity range, compound ZrB_2 has a narrow homogeneity range with values B/Zr, varying within $2.00 \le B/Zr \le 2.125$ [32] (Fig. 8). Moreover, at temperatures close to melting, this single-phase region becomes even narrower, ending with congruent melting ZrB_2 .

Elemental analysis of sample No. 1 (see Table 2) showed that the bulk of the sample contains excess boron (B/Zr \approx 2.72) unlike sample No. 2. On the phase diagram, this composition is shifted to the left relative to the stoichiometric composition ZrB_2 (B/Zr = 2; Zr 33.3 at%) and corresponds to zirconium content of 26.9 at%. Under equilibrium heating, such composition should completely melt at the liquidus temperature of 3423 K on the phase diagram. The melting onset temperature (3440 K) obtained during pulse heating of sample No. 1 coincides with the liquidus temperature given by the phase diagram.

For stoichiometric composition, the liquidus temperature is 3517 K (Fig. 8). Sample No. 2, having such composition, began melting at 3400 K, i.e., 117 K below the liquidus temperature, which, however, (considering the emissivity error) does not exceed the measurement uncertainty limits. Thus, in this case too, the melting onset temperature agrees with the phase diagram.

Under equilibrium conditions, the diboride melting should occur at a fixed temperature.

Experience shows (see below) that during rapid heating by a current pulse, the melting temperature of the substance coincides with the melting temperature during stationary heating. However, the measured surface temperature of the sample during its melting increases by 270 K (up to 3710 K) for sample No. 1 and by 350 K (up to 3750 K) for sample No. 2 (see

Fig. 4). Visually on thermograms, the melting plateau appears inclined (see Fig. 4).

Based on experimental study of this issue for metals (appearance of inclined melting plateau [4, 17, 33]) it can be assumed that the same mechanism operates in the case of diboride heating: 1) during current heating, sample melting begins from the surface and propagates into the sample depth; 2) during the melting of the sample volume, there is slight heating by current of the surface liquid layer above the melting point. The liquid layer on the surface may have a slightly higher temperature.

The onset of sample melting from the surface can be explained by increased defectiveness of its structure [4]. As known, grain boundaries also have increased defectiveness. It can be assumed that melting inside the sample begins along grain boundaries. Moreover, the larger the grains, the greater the difference in melting time between the surface and the entire sample volume. For metallic samples with small grain sizes, the surface temperature during melting increases by no more than 20 degrees [4]. For sintered ceramics, as we see in the example ZrB₂, this effect can reach hundreds of degrees. Let's estimate the heating time of a grain in ceramics ZrB₂:

$$t = l^2/a, (6)$$

where $a \approx 1.6 \cdot 10^{-5} \,\mathrm{m}^2/\mathrm{s}$ [28] — thermal diffusivity, $l \approx 10 \,\mu\mathrm{m}$ — half of the grain size. We obtain $t \approx 6 \,\mu\mathrm{s}$ i.e., indeed, a long time is required, comparable to the heating time of the entire sample.

Under real conditions, heat generation occurs both at grain boundaries and within grains, and heating time reduces to approximately 0.9 μ s (in Fig. 4 this is the duration of the melting plateau). Using expression (6), let's estimate the thickness l^* of the sample surface layer with elevated temperature. For melting time $t \approx 0.9$ μ s at the same thermal diffusivity, we obtain $l^* \approx 4$ μ m, which is only 3% of the sample thickness.

For ceramic sample studies using the current pulse heating method, samples with the minimum possible grain size are more preferable, which should reduce the sample melting time and decrease the surface temperature rise effect during its melting. In this regard, the development of sol-gel technology for obtaining compounds with a very fine fraction [12] is

one of the ways to solve this problem, i.e., obtaining homogeneous state during rapid microsecond heating.

The appearance of an inclined melting plateau may also be caused by possible changes in the emissivity of the substance during melting, which requires separate consideration.

In the case of carbides and nitrides with wide homogeneity regions (ZrC, HfC, TaC) a large melting interval is possible for another reason: melting will occur according to the phase diagram upon reaching the solidus temperature (beginning of the melting interval on the thermogram) and end at the liquidus temperature – the end of the melting interval, for example, as was the case for ZrC [34].

The melting region ZrB_2 is also visible on the dependence of input energy on temperature (see Fig. 5). The heat of fusion $\Delta E = E(T_{m2}) - E(T_{m1})$, calculated from the dependence E(T), was $\Delta E \approx 1.27$ kJ/g and $\Delta E = 1.28$ kJ/g (143 and 144 kJ/mol) for the first and second samples respectively.

Fig. 5 also shows the enthalpy versus temperature dependencies [25, 26], obtained by calculation — extrapolation of lower temperature data. The melting temperature in these works is taken as 3323 K [26] and 3313 K [25]. Our enthalpy data have a steeper temperature dependence than the calculated data, intersect them in the temperature range 2700 - 3700 K and diverge from them at higher temperatures by values exceeding measurement uncertainties. The calculated heat of fusion ZrB_2 in works [25, 26] is approximately 1.4 times lower and equals 0.927 ± 0.185 kJ/g (104.67 ± 20.93 kJ/mol) [25] and 0.927 kJ/mol (104.7 kJ/mol) [26].

5.3. Heat Capacity ZrB₂

In the dependence $C_p(T)$ (see Fig. 6), two coinciding peaks corresponding to the melting of two samples melting are visible. The melting region ZrB_2 (for sample No. 1) is shown by vertical dashed lines, where calculation using formula (3) does not work [15]. The obtained values $C_p \approx 2$ J/g of solid and liquid phases near the transition region are approximately twice as high as the calculated extrapolated data [25, 26]. This discrepancy may have several causes, one of which is the presumed formation of Frenkel defects. In the calculation work [35], very high energies of vacancy formation and Frenkel defects in ZrB_2 , of about 10 eV. were obtained. This factor is probably the main one giving

high values C_p . The small excess of boron in sample No. 1 composition does not significantly affect C_p — the curves for two samples coincide. When analyzing the reasons for discrepancy with reference data, the errors in extrapolation of calculated values should also be considered [25, 26]. The influence of impurities is also possible.

In the dependence $C_p(T)$ (see Fig. 6), a characteristic rise C_p before melting and sharp decrease after melting are visible. These features in heat capacity behavior can be qualitatively explained using the hypothesis about preferential formation of Frenkel defects during rapid substance melting [3]. When studying metal properties (W, Ta, Mo, Nb) under conditions of rapid current heating [3], two new effects were revealed: increase in isobaric heat capacity before melting and increase in electronic emission of metals under the same heating conditions and in the same temperature range. To explain these phenomena, work [3] proposed a hypothesis that under rapid heating conditions (units to tens of microseconds), along with the slow process of vacancy formation, the main role is played by the formation of Frenkel defects (interstitial atom + vacancy), which does not require movement (diffusion) of point defects over distances of grain size order and therefore proceeds much faster. The formation energy of a Frenkel defect is higher than the formation energy of two vacancies. For example, the vacancy formation energy in copper is 1 eV, while for a Frenkel defect it is 3 eV.

Non-equilibrium phenomena — emission and heat capacity anomalies — were detected during pulse experiments only in a relatively narrow temperature range near the melting point of metals. For example, after rapid melting of zirconium ([4], p. 84), the elevated heat capacity of liquid Zr decreases in the range 2100—2300 K to equilibrium values. The experiment shows that the effect of increased heat capacity for various substances disappears in the liquid region within 2–3 µs after melting.

In a recently published work [11], it was noted that for all carbides studied under rapid current heating, a sharp increase in the specific heat capacity of the solid phase was observed at temperatures 200–300 K lower than the melting temperature. The same effect was previously observed during rapid current heating of carbon [10] and it is observed in the present study of zirconium diboride (see Fig. 6). The authors suggest that this effect may be associated with the formation of Frenkel pair defects under rapid heating conditions,

as it is known that before melting, the concentration of defects in a crystalline body increases, and among all known crystal defects, Frenkel pairs require the least time to form. An important fact is the proof of independence of the melting temperature of metals [8], carbides [11], and carbon [36, 37] from the heating rate. Recent molecular dynamics estimates for zirconium carbide [38] (unrelated to rapid heating) at T = 3200 K (approximately 200 K before the onset of melting) show the possibility of heat capacity increase due to the formation of Frenkel pairs even before the solid melts. The abovementioned data is based on the physical picture of substance behavior presented in Frenkel's work [39].

The monograph [40] provides an expression for estimating the time to establish equilibrium concentration of thermal vacancies τ

$$\tau \simeq \left(\frac{L}{\delta}\right)^2 \frac{6\tau_0}{10} \exp\left(\frac{W}{k_B T}\right),\tag{7}$$

where L is the characteristic body size, δ is the width of the potential barrier, approximately equal to the atom size, $\tau_0 \sim 10^{-13}\,\mathrm{s}$ is the period of atomic oscillations, W is the activation energy of self-diffusion. The estimation [40] showed that for $L\simeq 1$ µm the establishment time is about $10^{-2}\,\mathrm{s}$. In our case, for $L\simeq 20$ µm (grain size), we get $\tau\sim 10^{-1}\,\mathrm{s}$, which is much longer than the heating time $(10^{-6}-10^{-5}\,\mathrm{s})$. Therefore, the formation of thermal vacancies under our conditions of rapid heating and melting can be neglected. In our opinion, the most probable process of lattice disordering before melting, its "dissociation" (Frenkel's term), is the process of Frenkel pair formation.

Note that under equilibrium conditions, the concentration of Frenkel defects is significantly lower than the concentration of vacancies due to the higher formation energy of Frenkel pairs. Let's estimate the ratio of these concentrations using copper as an example.

The concentrations of vacancies (Schottky defects) c_S and Frenkel defects c_F are equal to [41]

$$c_S \approx \frac{n}{N} \sim \exp\left(-\frac{W_S}{k_B T}\right),$$
 (8)

$$c_F \approx \frac{n}{\sqrt{NN^*}} \sim \exp\left(-\frac{W_F}{2k_B T}\right),$$
 (9)

where n is the number of vacant lattice sites (for Schottky defects), or the number of Frenkel defects, N is the total number of sites, W_S is the vacancy

T, K	C_p , J/(g · K)	C_p , J/(mol · K)	C_{v} , J/(mol · K)	C_{el} , J/(g · K)
3000	2.0	230	190	2.8
3440	2.7	300	240	_
3710	2.5	280	220	_
5000	_	_	_	4.7

Table 4. Isobaric, isochoric and electronic heat capacities of zirconium diboride

formation energy, N^* is the number of interstitial sites, W_F is the energy of moving an atom from a lattice site to an interstitial position. Assuming $N^* \approx N$, for the ratio of these concentrations we get

$$\frac{c_S}{c_F} \sim \exp\left(\frac{W_F - 2W_S}{2k_B T}\right). \tag{10}$$

At copper's melting point $(T=1356 \text{ K}, W_F=3 \text{ eV}, W_S=1 \text{ eV})$ we get $c_S/c_F\approx 10^2$, i.e., the concentration of Frenkel defects is much lower than the concentration of vacancies. At lower temperatures, this ratio increases, meaning the concentration of Frenkel defects under equilibrium conditions is negligibly small compared to the concentration of thermal vacancies throughout the entire range of solid phase existence.

The obtained data allow us to evaluate the isochoric heat capacity C_{ν} . For this, we will use the Nernst-Lindemann relation for crystalline solids [42]:

$$C_{v} = C_{p} - AC_{p}^{2}T, \tag{11}$$

where A is a constant that can be estimated using the formula

$$A = \frac{1}{5C_{pm}T_m},$$

see [42], where C_{pm} and T_m are the heat capacity at the melting point and the melting temperature. Let's perform estimates for sample No. 1, for which $T_m = 3440\,$ K. The increase in heat capacity C_p before melting and its decrease after melting make it difficult to estimate at the melting point. For this purpose, we will approximate $C_p(T)$ in the liquid phase in the temperature range $3820-4890\,$ K with a linear dependence (in this interval, the sharp decrease in C_p has ended):

$$C_p[J/(g \cdot K)] = 5.17 - 7.2 \cdot 10^{-4} T,$$

and at the melting point we get $C_{pm} = 2.69 \,\mathrm{J/(g\cdot K)}$, or $C_{pm} = 300 \,\mathrm{J/(mol\cdot K)}$. The estimation of C_v for

the solid phase is given in Table 4, which also provides its estimation using formula (11) for the liquid phase near the melting point. The basis for estimating the heat capacity of the liquid phase using the relationship obtained for solid crystalline substances is the known similarity of thermal expansion coefficients, heat capacity, and compressibility of solid and liquid phases of crystalline bodies in the melting region.

The estimation of the electronic component of heat capacity is performed using the formula

$$C_{el} = \gamma T, \tag{12}$$

where $\gamma = 0.93 \cdot 10^{-3} \, \text{J/(mol \cdot K}^2)$ [43] is the electronic heat capacity coefficient of the diboride, measured at temperatures 1.5–18 K. The low value of C_{el} is associated with the low value of γ for zirconium diboride compared to borides of other metals of groups IV-VI, for which it is units of mJ/(mol · K²) [43].

5.4. Electrical Resistance ZrB₂

The specific electrical resistance of two types of samples practically coincided in the temperature range 2000-4200 K (see Fig. 7). Previously, when studying ZrC, HfC, TaC samples, obtained by spark plasma sintering, it was established that the dependencies $\rho(T)$ in the solid phase have an unusual bell-shaped appearance with a maximum around 0.8 T_m and have a clearly expressed transition of the sample to the liquid phase [11]. An explanation was proposed: such dependency pattern is caused by additional sintering of samples during the experiment with pulse heating. For sintered samples ZrB₂ such effects are absent, the melting region ZrB₂ (for sample No. 1), shown in Fig. 7 by dashed lines, has no peculiarities. In the melting region, the resistance of the liquid phase is 192.6 $\mu\Omega$ · cm, solid phase – 177.6 $\mu\Omega$ · cm, their ratio is approximately 1.08.

6. CONCLUSIONS

Using the rapid pulse heating method, heating thermograms were obtained and temperature dependencies of enthalpy, heat capacity, and specific electrical resistance of zirconium diboride were measured in the temperature range of 2500-5000 K. Studies were performed on two types of samples: 98.7% purity with excess boron (B/Zr \approx 2.72) 99.9% purity of stoichiometric composition (B/Zr \approx 1.99). Data for the liquid phase were obtained for the first time. The study showed that differences in composition and structure of samples had little effect on their properties. Assuming that the emissivity ZrB₂ equals 0.7, the melting onset temperature of diboride 3400-3440 K, was obtained, which is consistent with the phase diagram of the B-Zr system. During the melting of samples, an increase in their surface temperature by 270–350 K above the melting onset was observed, associated with the peculiarity of ceramic structure – large grain size (up to $20-30 \mu m$).

The measured heat of fusion ZrB₂, equal to 1.28 kJ/g (144 kJ/mol), is higher than the estimated data provided in reference books. The result of heat capacity measurement in the solid phase (approximately $2 J/(g \cdot K)$ at 300 K) is higher than reference data. In the liquid phase, the heat capacity ZrB₂ decreases from 2 to approximately 1.5 J/g · K. An increase in heat capacity before melting and its sharp decrease after melting were noted. The same effect was previously observed during rapid heating of carbides [11]. Presumably, these effects are associated with the formation of Frenkel defects. The hypothesis about their determining role was considered in work [3] to explain the effects discovered in experiments with metals – a significant increase in electron emission and heat capacity just before melting of rapidly heated metal and rapid decrease in metal heat capacity after melting completion.

FUNDING

This work was supported by the Russian Science Foundation (grant No. 19-79-30086-P). The authors are grateful to G.E. Valyano (JIHT RAS) for analyzing the microstructure and composition of samples.

REFERENCES

1. E. Wuchina, E. Opila, M. Opeka, W. Fahrenholtz, and I. Talmy, Electrochem. Soc. Interface 16, 30 (2007).

- **2.** *V. A. Palekha, A. A. Getman, Boron. Properties and Applications in Nuclear Energy*, Naval Polytechnic Institute, Saint Petersburg (2017).
- 3. S.V. Lebedev, A.I. Savvatimskiy, UFN 144, 215 (1984).
- **4.** A.I. Savvatimskiy, V.N. Korobenko, High-Temperature Properties of Nuclear Power Metals (Zirconium, Hafnium and Iron at Melting and in Liquid State), MPEI Publishing House, Moscow (2012).
- **5.** *G.I. Mozharov*, PhD Thesis in Physics and Mathematics, IVTAN, Moscow (1983).
- **6.** V.N. Korobenko, O.A. Polyakova, A.I. Savvatimskiy, TVT **43**, 39 (2005).
- 7. V.Ya. Chekhovskoy, V.E. Peletskiy, TVT 47, 371 (2009).
- **8.** *S.V. Onufriev, A.I. Savvatimskiy, and A.M. Kondratyev*, High Temp.-High Press. **43**, 217 (2014).
- **9.** *V.N. Korobenko and A.I. Savvatimskiy*, J. NonCrystalline Sol. **205–208**, 672 (1996).
- **10.** A.I. Savvatimskiy, S.V. Onufriev, UFN **190**, 1085 (2020).
- **11.** *A.I. Savvatimskiy, S.V. Onufriev, N. M. Aristova*, UFN **192**, 642 (2022).
- **12.** *E.P. Simonenko*, Doctoral Thesis in Chemistry, IGIC RAS, Moscow (2016).
- **13.** *A.I. Savvatimskiy, S.V. Onufriev*, Nuclear Physics and Engineering **6**, 622 (2015).
- **14.** *S.V. Onufriev*, Bull. Russ. Acad. Sci. Phys. **82**, 430 (2018).
- **15.** *S.V. Onufriev, A.I. Savvatimskiy*, High Temperature **56**, 704 (2018).
- **16.** *Physical Quantities*. Handbook ed. by I.S. Grigoriev, E.Z. Meilikhov, Energoatomizdat, Moscow (1991).
- **17.** *V.N. Korobenko*, PhD Thesis in Physics and Mathematics, JIHT RAS, Moscow (2001).
- **18.** *A.N. Vinnikova, V.A. Petrov, A.E. Sheindlin*, High Temperature **8**, 1098 (1970).
- **19.** T.R. Reithgof and V.F. De Santis, in Measurement of Termal Radiation Properties of Solids, ed. by J.C. Richmond and D.C. Wash, NASA, SP-31 (1963).
- 20. F.H. Morgan, J. Appl. Phys. 22, 108 (1951).
- **21.** *T.I. Serebryakova, Yu.B. Paderno, G.V. Samsonov*, Optics and Spectroscopy **8**, 410 (1960).
- 22. V.S. Fomenko, G.V. Samsonov, Refractories 1, 40 (1962).
- **23.** *G.V. Samsonov, T.I. Serebryakova, V.A. Neronov*, **Borides**, Atomizdat, Moscow (1975).
- **24.** L.N. Latyev, V.A. Petrov, V.Ya. Chekhovskoy, E.N. Shestakov, Radiative Properties of Solid Materials, ed. by A.E. Sheindlin, Energia, Moscow (1974).
- **25.** H.L. Schick, Thermodynamics of Certain Refractory Compounds, Academic Press, New York-London, (1966), Vol. 1, 2.
- **26.** *M.W. Chase Jr.*, NIST-JANAF *Thermochemical Tables, Forth edition*, J. Phys. Chem. Ref. Data, Monogr. **9**, 1951 (1998).

- 685 (2023).
- **28.** J.W. Zimmermann, G.E. Hilmas, and W.G. Fahrenholtz, J. Am. Ceram. Soc. 91, 1405 (2008).
- 29. A. Ubbelohde, Melting and Crystal Structure, Mir, Moscow (1969).
- **30.** S.V. Onufriev, A.I. Savvatimskiy, and S.A. Muboyadzhyan, Mater. Res. Express 6, 125554 (2019).
- 31. Ya.B. Zeldovich, Yu.P. Raizer, Physics of Shock Waves and High-Temperature Hydrodynamic Phenomena, Nauka, Moscow (1966).
- **32.** *H. Okamoto*, J. Phase Equilibria **14**, 262 (1993).
- 33. S.V. Lebedev, A.I. Savvatimskiy, N.V. Stepanova, High Temperature 25, 912 (1987).
- **34.** A.I. Savvatimskiy, S.V. Onufriev, and S.A. Mubovadzhvan, J. Mater. Res. 32, 1287 (2017).
- 35. S.C. Middleburgh, D.C. Parfitt, P.R. Blair, and R.W. Grimesw, J. Am. Ceram. Soc. 94, 2225 (2011).

- 27. S.V. Onufriev, A.I. Savvatimskiy, High Temperature 61, 36. A.I. Savvatimskiy, Graphite Melting and Properties of Liquid Carbon, Fizmatkniga, Moscow (2014).
 - 37. A.I. Savvatimskiy, Carbon at High Temperatures. Springer Ser. in Mater. Sci. 134 (2015).
 - 38. T.A. Mellan, A. I. Duff, and M. W. Finnis, Phys. Rev. B **98**, 174116 (2018).
 - 39. Ya.I. Frenkel, Kinetic Theory of Liquids, Nauka, Leningrad (1975).
 - **40.** L.P. Filippov, Measurement of Thermal Properties of Solid and Liquid Metals at High Temperatures, Moscow State University Publishing, Moscow (1967), p. 268.
 - 41. Ch. Kittel, Introduction to Solid State Physics, Nauka, Moscow (1978).
 - 42. D.Sh. Tsagareishvili, Methods for Calculating Thermal and Elastic Properties of Crystalline Inorganic Substances, Metsniereba, Tbilisi (1977), p. 92.
 - 43. Y.S. Tvan, L.E. Toth, and Y.A. Chang, J. Phys. Chem. Solids 30, 785 (1969).